



On the effect of mean flow profile, wavelength and array length on focal-resolution of a quadrupole source using aeroacoustic time-reversal

Akhilesh Mimani¹; Con J. Doolan²; Paul R. Medwell³

^{1,2,3}School of Mechanical Engineering, The University of Adelaide, South Australia – 5005, Australia

ABSTRACT

This paper analyses the effect of the mean flow field, source wavelength and array length on the focal-resolution characteristics of an idealised lateral quadrupole source obtained using aeroacoustic Time-Reversal (TR). The TR simulations were implemented by numerically solving the 2-D Linearised Euler Equations (LEE) and enforcing the time-reversed acoustic pressure (stored during forward simulation) at the nodes of two Line Arrays (LAs) located outside the flow and on opposite sides. The TR simulation in a stationary medium and in a uniform mean flow indicates that interaction between the converging and diverging waves in the vicinity of quadrupole focal spots perpendicular to the LAs leads to the reinforcement of acoustic power at these regions. This results in formation of side-lobes of a relative magnitude larger than the quadrupole focal spots in the source maps, thereby making it difficult to characterise a quadrupole. During TR simulation of a quadrupole in a fully-developed non-uniform shear flow, refraction of the back-propagated waves through the shear-layer forces the acoustic fluxes to be focused almost completely at the focal spots, thereby significantly improving the quadrupole focal-resolution characteristics.

Keywords: Source localisation and transmission paths (74.6), Processing by microphone arrays (74.7), Quadrupoles (21.1.3) and Refraction and focusing (23.3)

1. INTRODUCTION

The acoustic Time-Reversal (TR) proposed by Fink *et al.* (1) is a robust method operating in the time-domain for localising and characterising aeroacoustic sources (2, 3). Padois *et al.* (2) used experimental acoustic pressure time-history data measured over one Line Array (LA) of microphones (located outside the flow) to localise a time-harmonic monopole source (modelled by a loudspeaker) and dipole source (simulated by two loudspeakers in proximity with their axis parallel to flow) in a wind tunnel flow using TR. The main limitation in their work is the use of only one LA of microphones which has a limited angular aperture and thus cannot record sufficient acoustic pressure data required for accurately characterising the flow-induced noise sources such as multipole aeroacoustic sources (4, 5). The present authors (3) have previously demonstrated that the use of a two LA configuration (shown in Fig. 1(a)) in a Time-Reversal-Mirror (TRM) during TR simulation is necessary and indeed, sufficient for characterising time-harmonic monopole and dipole (with axis perpendicular to mean flow) sources in a uniform mean flow field. However, it was observed that use of only two LAs of length equal to the breadth of the domain resulted in poor characterisation of the lateral quadrupole source due to a limited effective angular aperture. In a recent communication (6), the authors have shown that a significant improvement in the focal-resolution of a tonal quadrupole source located in a non-uniform mean shear flow is obtained by increasing the length of the two LAs (configuration shown in Fig. 1(a)) during TR because it results in a significantly larger effective angular aperture observed at the source.

An analysis of the accuracy of TR in localising and characterising a quadrupole source is important because the dominant/fundamental noise sources in a free-jet are thought to be (according to Lighthill's acoustic analogy (5)) due to convecting eddies having a quadrupole nature that are random both in space and time. Furthermore, the traditional source localisation techniques such as aeroacoustic beamforming (7)

¹akhilesh.mimani@adelaide.edu.au ²con.doolan@adelaide.edu.au ³paul.medwell@adelaide.edu.au

depend on *a-priori* assumption of the source characteristics. While beamforming can be used in the time-domain, it is most often used in the frequency-domain enabling the use of resolution improvement techniques (such as DAMAS or CLEAN-SC) to improve the interpretation of the results. However, beamforming represents the source statistically; therefore, it cannot yield valuable spatio-temporal evolution characteristics of acoustic fields. In fact, the authors have shown (6) that characterisation of a quadrupole using beamforming is limited due to high relative magnitude of side-lobes directly upstream of the source.

Time-Reversal, on the other hand, does not need to assume a source-type and is able to provide super-resolution of the source (8, 9), better than beamforming. It can also include the effect of scattering surfaces and model geometry to further improve the interpretation of results. Therefore, TR is potentially a superior method to investigate the spatio-temporal resolution of aeroacoustic sources. Indeed, it has a great potential in characterising the quadrupole and thus, can possibly be used to obtain accurate representations of the source maps of the flow-induced noise due to a free-jet. In a recent work (10), it was shown that for low Mach number flows; the dipole source nature (at the Aeolian tone (4)) of the flow-induced noise due to a cylinder in cross-flow can be obtained on neglecting the mean flow during TR simulation. Therefore, in light of the discussion on the source nature in a free-jet and recent TR results using experimental data (10), this work investigates using numerical experiments, effect of the mean flow profile (or a stationary medium) and the source wavelength on the focal-resolution of a quadrupole for a given length of the two LAs.

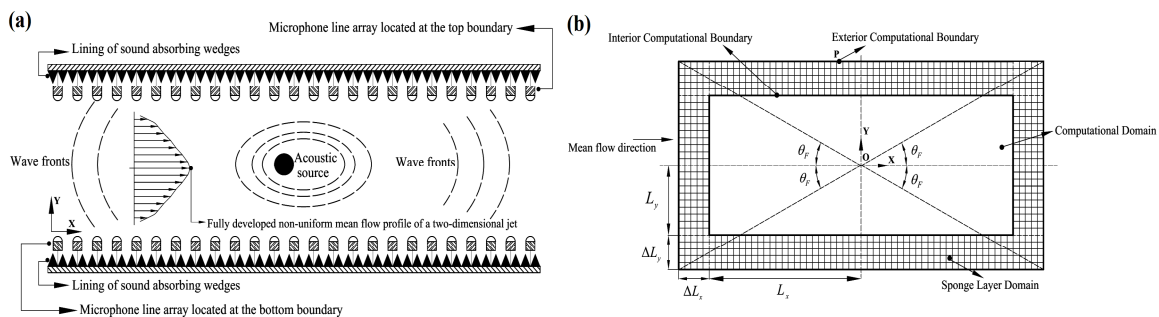


Figure 1 – (a) Schematic of the simulated set-up: Two microphone LAs located at the top and bottom boundaries of an anechoic wind tunnel for intercepting and recording the acoustic pressure field radiated by an aeroacoustic source. (b) A 2-D rectangular computational domain surrounded by a sponge-layer domain.

2. IMPLEMENTATION OF NUMERICAL SIMULATIONS: METHODOLOGY

The numerical implementation of the forward and TR simulations of acoustic wave propagation on a 2-D domain (schematically shown in Fig. 1(b)) are briefly described. The computational domain is completely enclosed by a sponge-layer domain which damps the incoming acoustic fluxes (waves), thereby minimising the reflections from the exterior computational boundaries and hence, its implementation is important for accurate modelling of a 2-D free-space (11). The half-lengths of the computational domain and the width of the sponge-layer domain are given by $L_x = 1.5$ m and $\Delta L_x = 0.15$ m along the x direction, respectively, $L_y = 0.5$ m and $\Delta L_y = 0.15$ m along the y direction, respectively. As indicated in Fig. 1(b), the direction of the subsonic mean flow is considered towards the positive x direction during the forward simulation. Equal mesh size given by $\Delta x = \Delta y = \Delta n = 0.005$ m is taken along the x and y directions, respectively. The number of nodes in the computational domain along the x and y directions is given by $N_x = (2L_x/\Delta x) + 1 = 601$ and $N_y = (2L_y/\Delta y) + 1 = 201$, respectively, whilst that in the sponge-layer along the x and y directions is given by $N_{\text{sponge}} = \Delta L_x/\Delta x = \Delta L_y/\Delta y = 30$, respectively.

2.1 Forward Simulation

The forward simulation of an idealised lateral quadrupole in a mean flow field is implemented by

numerically solving the inhomogeneous 2-D Linearised Euler Equations (LEE) in the Pseudo-Characteristic Formulation (11, 12), (known as the PCF) assuming homoentropic flow conditions.

$$\begin{aligned} \frac{\partial \tilde{p}}{\partial t} &= -\frac{\rho_0 c_0}{2} \left\{ (X_{\text{linear}}^+ + X_{\text{linear}}^-) + (Y_{\text{linear}}^+ + Y_{\text{linear}}^-) \right\} + c_0^2 S_1, \\ \frac{\partial \tilde{u}}{\partial t} &= -\frac{1}{2} (X_{\text{linear}}^+ - X_{\text{linear}}^-) - \tilde{v} \frac{\partial U_0}{\partial y} + \frac{S_2}{\rho_0}, \quad \frac{\partial \tilde{v}}{\partial t} = -\frac{1}{2} (Y_{\text{linear}}^+ - Y_{\text{linear}}^-) - U_0 \frac{\partial \tilde{v}}{\partial x} + \frac{S_3}{\rho_0}, \end{aligned} \quad (1a-c)$$

$$\text{where } X_{\text{linear}}^\pm = \pm (c_0 \pm U_0(y)) \left(\frac{1}{\rho_0 c_0} \frac{\partial \tilde{p}}{\partial x} \pm \frac{\partial \tilde{u}}{\partial x} \right) \text{ and } Y_{\text{linear}}^\pm = \pm c_0 \left(\frac{1}{\rho_0 c_0} \frac{\partial \tilde{p}}{\partial y} \pm \frac{\partial \tilde{v}}{\partial y} \right), \quad (2, 3)$$

$\tilde{p}(x, y, t)$, $\tilde{\rho}(x, y, t)$, $\tilde{u}(x, y, t)$ and $\tilde{v}(x, y, t)$ are the acoustic pressure (Pa), acoustic density ($\text{kg} \cdot \text{m}^{-3}$) and acoustic particle velocities ($\text{m} \cdot \text{s}^{-1}$) along the x and y direction, respectively, ρ_0 is the ambient density, taken equal to $1.21 \text{ kg} \cdot \text{m}^{-3}$, $c_0 = 343.14 \text{ m} \cdot \text{s}^{-1}$ is the sound speed (assuming isentropic process), t is the forward time (s). In Eqs. (1a-c), $U_0(y)$ denotes the subsonic mean flow velocity (towards the positive x direction), either (1) uniform over the domain so that $U_0 = 0.3c_0$ or (2) fully-developed non-uniform profile of a 2-D jet modelled with a Bickley's profile given by (13)

$$U_0(y) = c_0 M_0 \operatorname{sech}^2 \left(\beta \frac{y}{2(L_y + \Delta L_y)} \right). \quad (4)$$

Here, $M_0 = 0.3$ is the maximum Mach number of the subsonic non-uniform mean flow (about which the 2-D Euler equations are linearised) and β is the non-dimensional steepness parameter or strength of the shear-layer. Furthermore, X_{linear}^+ denotes the acoustic flux propagating towards the positive x direction with an enhanced speed of $(c_0 + U_0)$, whilst X_{linear}^- denotes the acoustic flux propagating towards the negative x direction with a reduced speed of $(c_0 - U_0)$, respectively. Similarly, Y_{linear}^\pm denotes fluxes propagating with towards the positive and negative y directions, respectively. The terms $\{S_1, S_2, S_3\}$ in Eqs. (1a-c) are the inhomogeneous source terms modelling a time-harmonic idealised lateral quadrupole source in the flow field. A lateral quadrupole source (with its axes perpendicular to the x and y directions) centred at the point (x_0, y_0) is modelled by first considering the Lighthill's tensor $[\mathbf{T}]$ of the form (6, 13).

$$[\mathbf{T}]_{2 \times 2} = \frac{F_Q}{\alpha_0} \begin{bmatrix} -\cos(\alpha_0(x - x_0))\delta(y - y_0) & 0 \\ 0 & \cos(\alpha_0(y - y_0))\delta(x - x_0) \end{bmatrix} \sin(\omega t), \quad (5)$$

defined over the domain given by $(x, y) \in [x_0 - \pi/2\alpha_0, x_0 + \pi/2\alpha_0] \times [y_0 - \pi/2\alpha_0, y_0 + \pi/2\alpha_0]$, where α_0 is a non-negative parameter determining the extent of the quadrupole source distribution domain. It is noted that $\omega = 2\pi f$ is the angular frequency ($\text{radian} \cdot \text{s}^{-1}$), f is the frequency (Hz) whilst $\delta(\cdot)$ signifies the Dirac-Delta function. The lateral quadrupole source is modelled by setting (6, 13)

$$\begin{aligned} \{S_1 \ S_2 \ S_3\}^T &= \left\{ 0 \ \frac{\partial T_{11}}{\partial x} + \frac{\partial T_{12}}{\partial y} \ \frac{\partial T_{21}}{\partial x} + \frac{\partial T_{22}}{\partial y} \right\}^T \\ &= F_Q \sin(\omega t) \times \left\{ 0 \ \sin(\alpha_0(x - x_0))\delta(y - y_0) \ -\sin(\alpha_0(y - y_0))\delta(x - x_0) \right\}^T, \end{aligned} \quad (6)$$

in Eqs. (1a-c). It is noted from Eq. (6) that the magnitude of the force distribution S_2 and S_3 is maximum at

$$\left\{ \begin{array}{l} x = x_0 \pm \pi/(2\alpha_0) \\ y = y_0 \pm \pi/(2\alpha_0) \end{array} \right\}, \text{ respectively, and zero at origin. Also, } \left\{ \begin{array}{l} S_2(x_0 + \pi/(2\alpha_0)) = -S_2(x_0 - \pi/(2\alpha_0)) \\ S_3(y_0 + \pi/(2\alpha_0)) = -S_3(y_0 - \pi/(2\alpha_0)) \end{array} \right\},$$

signifies that the force distributions S_2 as well as S_3 are of exactly opposite phase at the points of maximum magnitude. A point-like quadrupole source behaviour is obtained from Eq. (6) by choosing α_0 such that the distance between the points of maximum magnitude is minimised. Therefore, for implementing a point-like lateral quadrupole source (with its axes perpendicular to the x and y directions), the pair of points given by (1) $(x_0 \pm \pi/(2\alpha_0), y_0)$ and (2) $(x_0, y_0 \pm \pi/2\alpha_0)$ must be separated by two nodes, implying $\alpha_0 = \pi/(2\Delta n)$ and that the quadrupole source domain equals $[x_0 - \Delta x, x_0 + \Delta x] \times [y_0 - \Delta y, y_0 + \Delta y]$, whilst the source terms S_2 and S_3 in Eq. (6), simplifies to

$$S_2(x = x_0 \pm \Delta x, y = y_0) = \pm F_Q \sin(\omega t), \quad S_3(x = x_0, y = y_0 \pm \Delta y) = \mp F_Q \sin(\omega t), \quad (7a, b)$$

and is set to zero at the remaining nodes in the source domain $[x_0 - \Delta x, x_0 + \Delta x] \times [y_0 - \Delta y, y_0 + \Delta y]$.

The spatial derivatives in fluxes propagating along the positive $(X_{\text{linear}}^+, Y_{\text{linear}}^+)$ and negative $(X_{\text{linear}}^-, Y_{\text{linear}}^-)$ directions are computed using overall upwind-biased FD schemes implemented as matrix-column multiplication shown as (6)

$$\frac{\partial \{\psi\}^+}{\partial n} \approx \frac{1}{\Delta n} [\mathbf{R}_1] \{\psi\} \quad \text{and} \quad \frac{\partial \{\psi\}^-}{\partial n} \approx \frac{1}{\Delta n} [\mathbf{R}_2] \{\psi\}, \quad (8, 9)$$

respectively, where $\{\psi\} = \{\psi_1, \psi_2, \psi_3, \dots, \psi_N\}^T$ represents either the acoustic pressure or the acoustic particle velocities. Here, $[\mathbf{R}_1]$ and $[\mathbf{R}_2]$ are the overall upwind-biased FD scheme matrices formulated using (a) 4th order, 7-point optimised upwind biased FD scheme of Zhuang and Chen (14) at interior nodes, (b) the 5th and 3rd order standard upwind-biased FD schemes near the boundary nodes, (c) the 7-point optimised one-sided FD scheme by Zhuang and Chen (14) at the penultimate nodes and (d) the 7-point optimised backward FD scheme of Tam (15) at the boundary nodes. It is noted that $\{\psi\}$ represents either the acoustic pressure or particle velocities, N stands for N_x or N_y and Δn represents Δx or Δy . It is noted that since the mean flow is assumed to be towards the positive x direction, the spatial derivative $c_0 M_0 (\partial \tilde{v} / \partial x)$ in Eq. (1c) is computed using Eq. (8). The 3rd order Total-Variation-Diminishing Runge-Kutta scheme (16) is used for time-integration during the forward and TR simulations. The time-step Δt is computed in accordance with the following Courant–Friedrichs–Lewy (CFL) condition (16).

$$CFL = \frac{(c_0 + \max(U_0)) \Delta t}{\Delta n} \leq 1. \quad (10)$$

In this work, $CFL = 0.2$ is considered to ensure accuracy of the forward and the TR simulations. Based on the geometrical and simulation parameters chosen, $\Delta t = 2.24175 \times 10^{-6}$ s. The first-order Clayton-Engquist-Majda (CEM) boundary conditions (17) were implemented at nodes on the $x = \pm (L_x + \Delta L_x)$ and $y = \pm (L_y + \Delta L_y)$ boundaries to model the anechoic boundary conditions (ABCs) whilst the special corner boundary conditions (18) were implemented at the four top corner nodes to locally

model the ABCs. In order to further suppress the spurious numerical reflections during the 2-D forward simulations, the incoming acoustic fluxes near the exterior computational boundary are damped over several nodes of a sponge-layer domain (11). The damping is implemented by multiplying the incoming fluxes with a Gaussian function which is unity at the nodes of the interior computational boundary and smoothly decays to zero at the nodes of the exterior computational boundary. The term $U_0(\partial\tilde{v}/\partial x)$ is also damped over the nodes of the sponge-layer domain and the condition $(\partial\tilde{v}/\partial x)|_{-L_x-\Delta L_x} = 0$ to suppress the incoming acoustic disturbances at $x = -L_x - \Delta L_x$ boundary that are advected by the mean flow, thereby preventing instability. It is noted that implementation of ABC (with or without the inclusion of sponge-layer domain) at the exterior boundaries of the 2-D computational domain is crucial for the temporal stability of forward simulation of a pulse propagating in a free-space over a large time duration. The forward simulations were carried out for a large time-interval $t = [0, T = N_{\max}\Delta t]$ during which the zero-initial conditions were replaced with several periods of time-harmonic response, whilst the acoustic pressure time-history was stored at all the nodes (or equivalently, virtual microphones of spacing equal to the mesh size) at the top ($y = L_y$) and the bottom ($y = -L_y$) interior boundaries after every time-step. Here, N_{\max} denotes the number of time-steps during forward simulation taken equal to 13000.

2.2 Time-Reversal (TR) Simulation

The TR simulation over the 2-D domain $(x, y) \in [-L_x, L_x] \times [-L_y, L_y]$ is implemented by setting the source terms to zero, reversing the mean flow direction (to account for the convective effect of mean flow, thereby ensuring TR invariance) and introducing the following transformations (2, 3, 6, 9, 19) in Eqs. (1-3)

$$t \rightarrow T - \tilde{t}, \quad \tilde{p}(x, y, t) \rightarrow \tilde{p}(x, y, \tilde{t}), \quad \tilde{u}(x, y, t) \rightarrow -\tilde{u}(x, y, \tilde{t}), \quad \tilde{v}(x, y, t) \rightarrow -\tilde{v}(x, y, \tilde{t}), \quad (11a-d)$$

to obtain the following set of time-reversed homogenous 2-D LEE in the PCF (6, 8, 9).

$$\begin{aligned} \frac{\partial \tilde{p}}{\partial \tilde{t}} &= -\frac{\rho_0 c_0}{2} \left\{ (\tilde{X}_{\text{linear}}^+ + \tilde{X}_{\text{linear}}^-) + (\tilde{Y}_{\text{linear}}^+ + \tilde{Y}_{\text{linear}}^-) \right\}, \\ \frac{\partial \tilde{u}}{\partial \tilde{t}} &= -\frac{1}{2} (\tilde{X}_{\text{linear}}^+ - \tilde{X}_{\text{linear}}^-) - \tilde{v} \left(-\frac{\partial U_0}{\partial y} \right), \quad \frac{\partial \tilde{v}}{\partial \tilde{t}} = -\frac{1}{2} (\tilde{Y}_{\text{linear}}^+ - \tilde{Y}_{\text{linear}}^-) - (-U_0) \frac{\partial \tilde{v}}{\partial x}, \end{aligned} \quad (12a-c)$$

$$\text{where} \quad \tilde{X}_{\text{linear}}^{\pm} = \pm (c_0 \mp U_0) \left\{ \frac{1}{\rho_0 c_0} \frac{\partial \tilde{p}}{\partial x} \pm \frac{\partial \tilde{u}}{\partial x} \right\} \quad \text{and} \quad \tilde{Y}_{\text{linear}}^{\pm} = \pm c_0 \left\{ \frac{1}{\rho_0 c_0} \frac{\partial \tilde{p}}{\partial y} \pm \frac{\partial \tilde{v}}{\partial y} \right\}, \quad (13, 14)$$

and \tilde{t} denotes the reverse time. It is noted that the time-reversed 2-D LEE given by Eqs. (12a-c) are identical to Eqs. (1a-c), except that the direction of subsonic mean flow is reversed in $\tilde{X}_{\text{linear}}^{\pm}$ fluxes which is essential to ensure TR invariance (2, 19). Furthermore, the derivative $(\partial\tilde{v}/\partial x)$ in Eq. (12c) is computed using Eq. (9) due to reversal of mean flow direction. The time-reversed acoustic pressure history was enforced as Dirichlet boundary conditions (2) at the boundary nodes corresponding to the top and bottom LAs after every time-step of TR simulation which initiates the back-propagation of acoustic waves from the two LAs into the domain. The first-order CEM ABCs and the corner ABCs were implemented at the computational boundaries $x = \pm L_x$ and $y = \pm L_y$ to eliminate spurious numerical reflections and stabilise the

2-D TR simulations. The ABCs were further reinforced by setting the incoming fluxes to zero at the computational boundaries, i.e., $\tilde{X}_{\text{linear}}^{\pm} = 0$ at $x = \mp L_x$, respectively, and $\tilde{Y}_{\text{linear}}^{\pm} = 0$ at $y = \mp L_y$, respectively.

The boundary condition $(\partial\tilde{v}/\partial x)|_{x=L_x} = 0$ was also implemented to eliminate the incoming spurious numerical waves advected by the fluid. A Time-Reversal-Sponge-Layer was implemented across the first 15 nodes adjacent to and including the node on the LA boundaries for suppressing the deteriorating effect of flux interference on TR simulation (6). The source location in the 2-D domain was obtained by determining the region(s) of maximum magnitude (termed as the focal spots) in the Root-Mean-Square time-reversed acoustic pressure field (3) denoted by $\tilde{p}_{RMS}^{TR}(x, y)$. The node at which focal spot is maximum is termed as the focal point. The $\tilde{p}_{RMS}^{TR}(x, y)$ field was converted to dB (with respect to $p_{ref} = 2 \times 10^{-5}$ Pa) and expressed relative to its magnitude at the focal point(s) given by the $\tilde{p}_{dB}^{TR}(x, y)$ field.

3. SOURCE MAPS: TR SIMULATION RESULTS AND DISCUSSION

The TR source maps of an idealised lateral quadrupole source (of a tonal frequency f) obtained using two LAs located at $y = \pm L_y$ boundaries are analysed to examine the effect of mean flow profile, frequency and array length on the focal-resolution characteristics. To this end, the following sets of parametric studies were carried out with the following default values (indicated by a line below each value) of tonal frequency $f = 3$ kHz, aspect-ratio $L_x/L_y = 3$ and steepness parameter $\beta = 10$.

(1) Mean flow profile: A stationary medium, a uniform mean flow of Mach number $M_0 = 0.3$ and a fully-developed non-uniform mean shear flow field given by Eq. (4) with different values of the parameter $\beta = \{1, 5, 10, 20, 40, 60\}$ was simultaneously considered during the forward simulation with the direction of the mean flow reversed during the TR simulation.

(2) Source maps corresponding to tonal frequencies $f = \{1.5, 3, 4.5, 6\}$ kHz were analysed.

(3) Source maps based on aspect-ratio $L_x/L_y = \{1, 2, 3, 4\}$ with two LAs located at $y = \pm L_y$ boundaries as well as the source map using a LA configuration completely enclosing the domain were analysed.

In each of the parametric studies, the centre of the 2-D domain (set to be the origin) is the known location, (indicated by a circle **O** in source maps), i.e., $x_0 = y_0 = 0$ whilst $F_0 = 100 \text{ N} \cdot \text{m}^{-2}$ in Eqs. (7a, b).

3.1 Effect of Mean Flow Profile

Figure 2(a) and (b) depict the source localisation maps using TR of an idealised lateral quadrupole source located in a stationary medium ($M_0 = 0$) and in a uniform mean flow ($M_0 = 0.3$) field, respectively, whilst Figs. 3(a-f) presents the quadrupole source maps in a non-uniform mean shear flow profile with steepness parameter $\beta = \{1, 5, 10, 20, 40, 60\}$ in parts (a) to (f), respectively. It is noted that the source maps are shown over the sub-domain $|x| \leq 0.5 \text{ m}$, $|y| \leq 0.5 \text{ m}$. The thick white lines in each of the source maps signify the presence of LAs at $y = \pm L_y$ boundaries, whilst the 'reversed' direction of mean flow is indicated by an arrow in Figs. 2(b) and 3(a-f). The quadrupole source nature in Figs. 2(a) and (b) is indicated by the formation of four focal spots in proximity and their geometrical center (indicated by a cross **X**) taken as the predicted source location demonstrates the accuracy of TR source localisation. However, the formation of side-lobes on the y axis (near $y = \pm 0.12 \text{ m}$) of a large relative magnitude (0 dB) tends to overwhelm or camouflage the four focal spots constituting the quadrupole and therefore, presents difficulty in characterising the quadrupole source nature, especially for the case of a uniform mean flow. Indeed, these side-lobes may be mistaken for the presence of a spurious source.

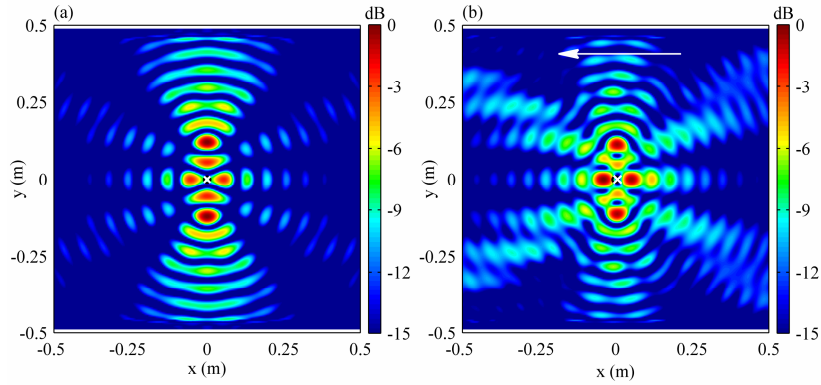


Figure 2 – Source localisation map (obtained using two LAs at $y = \pm L_y$ boundaries) of an idealised quadrupole source ($f = 3$ kHz) located in (a) a stationary medium and (b) a uniform mean flow.

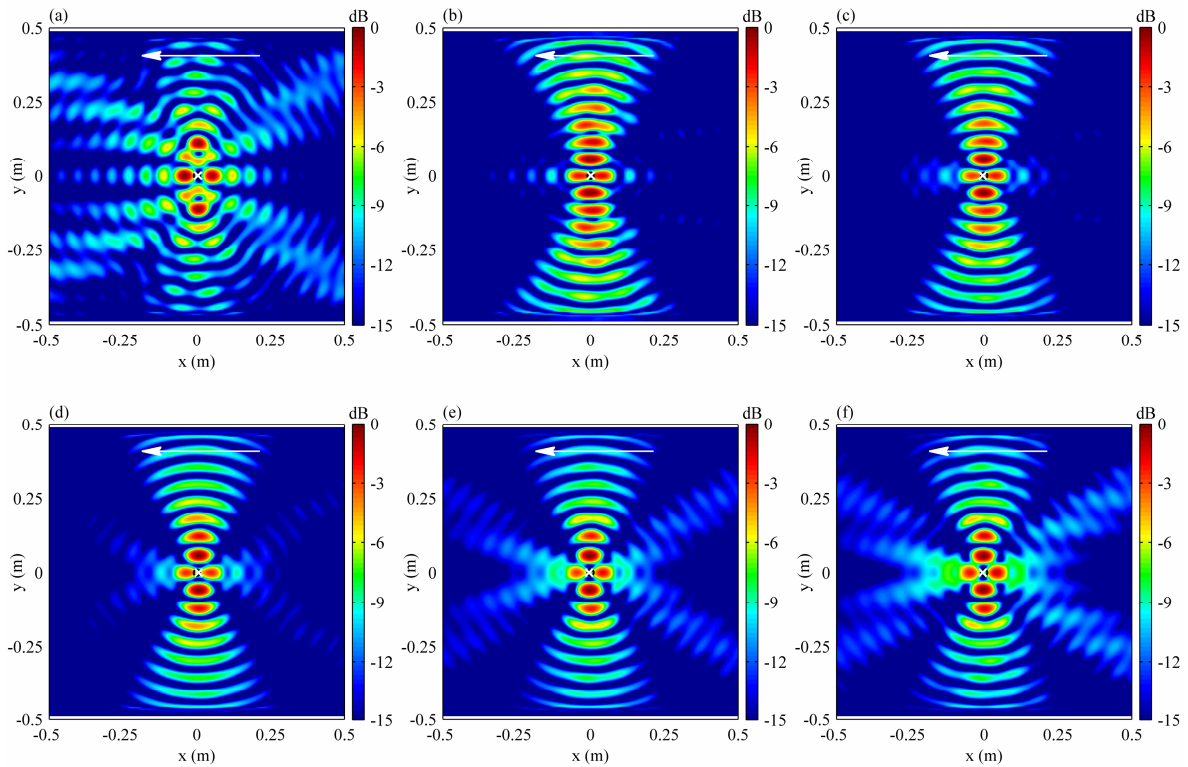


Figure 3 – Source localisation map (obtained using two LAs at $y = \pm L_y$ boundaries) of an idealised quadrupole source ($f = 3$ kHz) located in a fully-developed non-uniform mean shear flow (given by Eq. (4)) with steepness parameter $\beta = \{1, 5, 10, 20, 40, 60\}$ in parts (a) to (f), respectively.

Figures 3(a-f) demonstrate a dramatic improvement in focal-resolution characteristics of the quadrupole source with an increase in the steepness parameter β keeping the frequency $f = 3$ kHz constant. This observation may be explained by correlating the source wavelength λ with the half-width y_0 of the shear-layer given by the following analytical expression.

$$U(y_0) = \frac{c_0 M_0}{2} \Rightarrow y_0 = 2 \times \operatorname{sech}^{-1} \left(\frac{1}{\sqrt{2}} \right) \times \frac{(L_y + \Delta L_y)}{\beta} = 1.7627 \times \frac{(L_y + \Delta L_y)}{\beta}. \quad (15)$$

For $\beta = \{1, 5, 10, 20, 40, 60\}$, the ratio of the half-width to the source wavelength ($\lambda = 0.1144$ m for frequency $f = 3$ KHz) is given by $y_0/\lambda = \{10.02, 2.00, 1.00, 0.50, 0.25, 0.17\}$ m, respectively. It is noted that for $\beta = 1$, $\lambda \ll y_0$, therefore, the source apparently observes an almost uniform mean flow

profile and as a result, the source map shown in Fig. 3(a) is nearly identical with that obtained in Fig. 2(b). For $\beta = 5$, $\lambda \approx 0.5y_0$, as a result, the source begins to experience the non-uniform nature of flow, therefore, the refraction effects are pronounced, leading to a significantly improved focal-resolution. With an increase in the value of β , for instance, $\beta = 10$, $y_0 \approx \lambda$, the refraction effects are stronger and with successively larger values of $\beta = \{20, 40, 60\}$, $\lambda \gg y_0$, thereby resulting in a strong refraction of acoustic waves. Under such rapidly varying shear-layer flows, there is a progressive improvement in resolution of the four focal spots, in particular, the relative magnitude of the side-lobes near the region $x = 0$, $y = \pm 0.12$ m is smaller than the top and bottom focal spots, resulting in a significantly improved source map. Furthermore, the formation of upstream and downstream focal spots is more pronounced, in particular, for $\beta = \{40, 60\}$, the upstream and downstream focal spots completely separate out which signifies a better focal-resolution.

On the basis of the foregoing observations and discussion, the following rule of thumb may be formulated: the focal-resolution of the quadrupole source map improves significantly when the source wavelength λ is much greater than or at least equal to the half-width y_0 of the shear-layer. This is because under strongly refractive flow conditions, a relatively large fraction of the acoustic waves/power and directivity information of waves is intercepted, subsequently recorded and played back from the top and bottom LAs during TR, thereby resulting in an improved TR focus.

The case of a stationary medium or a uniform flow field may be re-discussed here, in such flow conditions, refraction is not observed, hence, the two LAs are able to record a limited acoustic pressure time-history data. Therefore, a significant portion of acoustic pressure data propagating through the upstream (left) and downstream (right) computational boundary during the forward simulation (emission from source) is unaccounted for. Hence, the interaction or interference of back-propagated acoustic waves near the quadrupole source location during TR simulation using only top/bottom LAs in such flow conditions is not able to satisfactorily recreate the four focal spots (constituting the quadrupole). Rather, due to a limited wave interaction near the source, relatively large side-lobes are observed in the quadrupole source maps which tend to overwhelm the four focal spots, making its characterisation difficult.

3.2 Effect of Source Wavelength

Figures 4(a-c) depict the source maps (over the sub-domain $|x| \leq 0.25$ m, $|y| \leq 0.25$ m) of a quadrupole of tonal frequencies $f = \{1.5, 4.5, 6\}$ kHz, respectively, in a mean shear flow with $\beta = 10$.

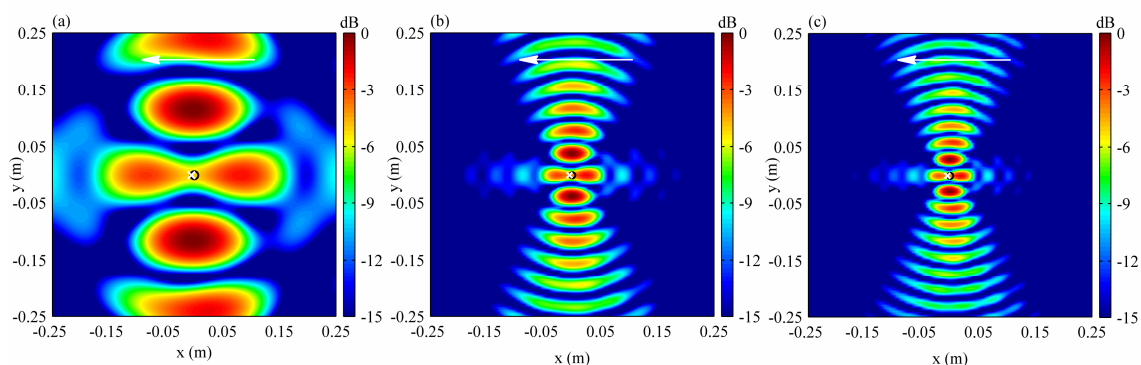


Figure 4 – Source localisation map (obtained using two LAs at $y = \pm L_y$ boundaries) of an idealised quadrupole source located in a fully-developed non-uniform mean shear flow (given by Eq. (4)) with $\beta = 10$ and source frequency $f = \{1.5, 4.5, 6\}$ kHz in parts (a) to (c), respectively.

It is noted that the half-width $y_0 = 0.1146$ m whilst the corresponding source wavelengths are given by $\lambda = [0.2288, 0.0763, 0.0572]$ m, respectively. This indicates that at $f = 1.5$ kHz (low frequency), the source wavelength is twice that of the half-width, therefore, an enhanced focal-resolution of the four focal spots is observed in the source map shown in Fig. 4(a). At higher frequencies, $f = 3$ kHz (map shown in Fig. 3(b)) and at $f = \{4.5, 6\}$ kHz, the source wavelength is smaller but comparable to the shear-layer half-width, therefore, the focal-resolution in the source maps shown in Figs. 4(b, c) are satisfactory. However, it is noted that the relative magnitude of the downstream focal-spot (with respect

to the *reversed* mean flow) in Fig. 4(c) is significantly smaller and in fact, appears to be merged or coalesced with the upstream focal spot. Numerical experiments or TR simulations revealed that the focal-resolution deteriorates at higher frequencies (with β constant) as the upstream and downstream focal spots tend to completely coalesce making it difficult to ascertain their individual existence.

3.3 Effect of Array Length: Partial versus Full Angular Aperture

The effect of increasing the effective angular aperture (by increasing the length of the top and bottom LAs or using a LA configuration completely enclosing the domain) on the focal-resolution of the quadrupole source is investigated. Figures 5(a-c) presents the source map of a quadrupole source located in a stationary medium, uniform mean flow field and shear mean flow, respectively, obtained using top and bottom LAs of aspect ratio $L_x/L_y = 4$ whilst parts (d-f) presents the corresponding source maps, respectively, obtained using a LA configuration completely enclosing the 2-D domain.

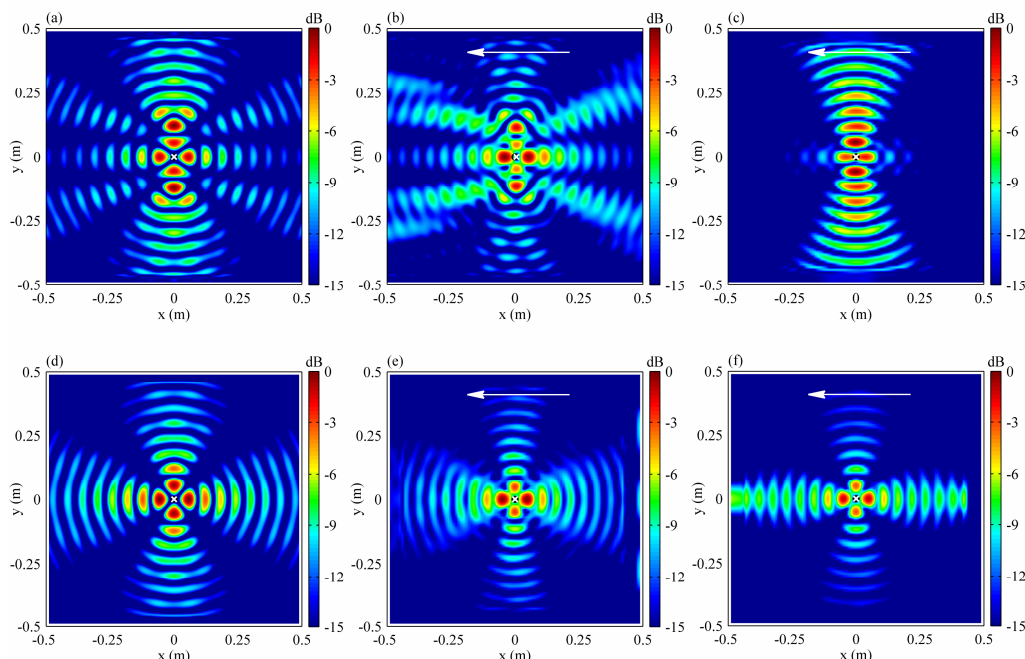


Figure 5 – Quadrupole source map $\{f = 3 \text{ kHz}\}$ in a stationary medium (parts **a** and **d**), a uniform mean flow field (parts **b** and **e**) and a non-uniform mean shear flow with $\beta = 10$ (parts **c** and **f**). The source maps in (a) to (c) are obtained using two LAs located at $y = \pm L_y$ boundaries with aspect-ratio $L_x/L_y = 4$ whilst a LA configuration completely enclosing the domain is used in (d) to (f).

It is observed from Figs. 5(a-c) that the focal-resolution, in general, improves only marginally on further increasing $L_x/L_y = 4$ from $L_x/L_y = 3$ (considered in Figs. 2(a, b) and 3(a-f)). In particular, it is noted that the relative magnitudes of the four focal spots in Fig. 5(a) and that of the top and bottom focal spots in Fig. 5(b) slightly increases, whilst the relative magnitude of the side-lobes in Fig. 5(b) diminishes slightly. Figures 5(d-f) depict the four focal spots of the quadrupole located in proximity that are completely separated from each other at their geometrical centre whilst the relative magnitude of the side-lobes immediately adjacent to the four focal spots are substantially lower. This demonstrates a LA configuration completely enclosing the source accounts for the waves propagating in all directions and its use takes into consideration a complete interaction of the back-propagated waves near the source, yielding the best possible resolution of the quadrupole (3).

4. CONCLUSIONS

The effect of the mean flow profile, source wavelength and the array length (the effective angular aperture) on the focal-resolution characteristics in the Time-Reversal (TR) source map of an idealised lateral quadrupole source is analysed in this work. While it was previously shown (3) that a relatively low source resolution of the quadrupole is obtained (in a uniform mean flow) using only two LAs located at the top and bottom boundaries with a small aspect-ratio $L_x/L_y = 1$, this paper demonstrates

that by considering a higher aspect-ratio $L_x/L_y = 3$ or more during TR simulation in a stationary medium or a uniform flow field, the source map improves due to the formation of four distinct focal spots constituting the quadrupole. However, the occurrence of side-lobes of a relative magnitude larger than or equal to the four focal spots in the source map tends to camouflage the focal spots, therefore making the characterisation of the quadrupole difficult. On using the same aspect-ratio $L_x/L_y = 3$ or more during TR in a non-uniform shear flow such that the wavelength λ is much greater than or at least equal to the half-width y_0 of the shear-layer, the relative magnitude of the side-lobes is significantly diminished due to refraction phenomenon whilst the four distinct focal spots are observed, thereby dramatically improving the focal-resolution characteristics. The observations reported in this paper will have an important role in designing Line-Array (LA) configurations (for TR simulations) during experiments on a free-jet and subsequently in analysing the TR source maps of the free-jet.

ACKNOWLEDGEMENTS

The Australian Research Council (ARC) is gratefully acknowledged for their support of this work through Discovery grant DP 120102134 ‘Resolving the mechanics of turbulent noise production’.

REFERENCES

1. Fink M, Cassereau D, Derode A, Prada C, Roux P, Tanter M, Thomas JL, Wu F. Time-reversed acoustics, *Rep Prog Phys.* 2000; 63(12): 1933-1995.
2. Padois T, Prax C, Valeau V, Marx D. Experimental localization of an acoustic source in a wind-tunnel flow by using a numerical time-reversal technique, *J Acoust Soc Am.* 2012; 132(4): 2397-2407.
3. Mimani A, Doolan CJ, Medwell PR. Multiple line arrays for the characterization of aeroacoustic sources using a time-reversal method, *J Acoust Soc Am.* 2013; 134(4): EL327-EL333.
4. Blake WK, *Mechanics of Flow-Induced Sound and Vibration*, NY, USA: Academic Press; 1986.
5. Lighthill MJ, On sound generated aerodynamically—I. General Theory, *Proc. R. Soc. Lond. Ser. A.* 1952; 211, 564–587.
6. Mimani A, Prime Z, Doolan CJ, Medwell PR. A sponge-layer damping technique for aeroacoustic time-reversal, Revision submitted to the *J Sound and Vib.*
7. Johnson DH, Dudgeon DE. *Array Signal Processing*, Englewood Cliffs, NJ, USA: Prentice Hall; 1993.
8. Mimani A, Doolan CJ, Medwell PR. Enhancing the focal-resolution of aeroacoustic time-reversal using a point sponge-layer damping technique, *J Acoust Soc Am.* 2014; 136(3): EL199-EL205.
9. Mimani A, Doolan CJ, Medwell PR. Enhancing the resolution characteristics of aeroacoustic time-reversal using a point-time-reversal-sponge-layer, *Proc 20th AIAA/CEAS Aeroacoustics Conference*; 16-20 June 2014; Atlanta, Georgia, USA, Paper No. 2316.
10. Prime Z, Mimani A, Moreau DJ, Doolan CJ. An Experimental comparison of beamforming, time reversal and near-field acoustic holography for aeroacoustic source localization, *Proc 20th AIAA/CEAS Aeroacoustics Conference*; 16-20 June 2014; Atlanta, Georgia, USA, Paper No. 2917.
11. Lu S-Yi, Sagaut P. Pseudo-characteristic formulation and dynamic boundary conditions for computational aeroacoustics, *Int J Numer Methods Fluids* 2007; 53(2): 201-227.
12. Sesterhenn J. A characteristic-type formulation of the Navier-Stokes equations for high order upwind schemes, *Comput. Fluids* 2001; 30(1): 37-67.
13. Bailly C, Juve D. Numerical solution of acoustic wave propagation problems using linearized Euler equations, *AIAA J.* 2000; 38(1): 22-29.
14. Zhuang M, Chen RF. Applications of high-order optimized upwind schemes for computational aeroacoustics, *AIAA J.* 2002; 40(3): 443-449.
15. Tam CKW, *Computational aeroacoustics: Issues and methods*, *AIAA J.* 1995; 33(10): 1788-1796.
16. Gottlieb S, Shu C-W. Total variation diminishing Runge-Kutta schemes, *Math Comput.* 1998; 67: 73-85.
17. Clayton R, Engquist, B. Absorbing boundary conditions for acoustic and elastic wave equations, *B Seismol Soc Am.* 1977; 67(6): 1529-1540.
18. Engquist B, Majda A. Radiation boundary conditions for acoustic and elastic wave calculations, *Commun Pur Appl Math.*, 1979; 32(3): 313–357.
19. Deneuve A, Druault P, Marchiano R, Sagaut P. A coupled time-reversal/complex differentiation method for aeroacoustic sensitivity analysis: towards a source detection procedure, *J Fluid Mech.* 2010; 642, 181-212.